Journal of the Korean Chemical Society
2013, *Vol. 57, No. 6*
Printed in the Republic of Korea
http://dx.doi.org/10.5012/jkcs.2013.57.6.661

속보 (Communications)

MnO_2 Nanoflakes and Nanothorns Deposited on Carbon Fiber Paper for Pseudocapacitor Electrode

Eun Joo Lee[†] and Jin Ho Bang[†,‡,*]

[†]*Department of Bionano Engineering, Hanyang University, 55 Hanyangdaehak-ro, Sangnok-gu, Ansan, Kyeonggi-do 426-791, Republic of Korea*
[‡]*Department of Chemistry and Applied Chemistry, Hanyang University, 55 Hanyangdaehak-ro, Sangnok-gu, Ansan, Kyeonggi-do 426-791, Republic of Korea. *E-mail: jbang@hanyang.ac.kr*
(Received October 28, 2013; Accepted November 12, 2013)

Key words: MnO_2, Pseudocapacitor, Capacitance, Energy storage

Along with lithium-ion batteries, supercapacitors have received great attention as a future energy storage system.[1] Despite the successful commercialization of electrical double layer capacitors (EDLCs), one type of supercapacitors, their utilization has been somewhat limited in comparison to lithium-ion batteries, which results mainly from their low energy densities.[2,3] To overcome such restriction, pseudocapacitors that resemble batteries in the charge storage mechanism have been intensively investigated over the last decades. A variety of transition metal oxides and hydroxides, such as MnO_2, Co_3O_4, $Co(OH)_2$, NiO, $Ni(OH)_2$, have been utilized as active electrode materials.[4] Among them, MnO_2 has received great attention because of its earth-abundance, low-cost, a high theoretical specific capacitance of ~1380 F/g.[5,6] Like other transition metal oxide materials, however, the practical application of MnO_2 in supercapacitors has been hindered due to its low electrical conductivity (10^{-5}–10^{-6} S/cm).[7] This drawback can be alleviated to some extent by mixing MnO_2 with activated carbon. However, this conventional procedure often leads to the aggregation of MnO_2, thus limiting the full utilization of MnO_2. Recent efforts to address this issue are such that MnO_2 is directly deposited onto various free-standing conductive substrates such as Ni foam, graphene foam, and carbon cloth to maximize the utilization of MnO_2 surface.[5,8,9] In this study, we employed a carbon fiber paper (CFP) as a substrate and directly grew MnO_2 on CFP via a simple hydrothermal reaction. Interestingly, we observed that different crystallographic structures of MnO_2 (α-MnO_2 and δ-MnO_2) were obtained depending on the presence or absence of a pre-treatment by Pt sputtering. We also found that these two MnO_2 species showed different specific capacitances when evaluated as pseudocapacitor electrodes.

δ-MnO_2 was prepared by a simple hydrothermal reaction. For the deposition of a seed layer, a piece of bare CFP (SGL Technologies) was dipped into a solution containing 0.03 M manganese acetate for 15 min and annealed at 450 °C for 30 min. The seeded CFP was dipped into an aqueous 71.2 mM $KMnO_4$ solution containing HCl (1 mL), and the whole solution (40 mL) was transferred to a 100 mL Teflon-lined stainless steel autoclave and heated at 120 °C for 1 h. The CFP was removed from the cooled autoclave and washed with deionized water to remove the unreacted species adsorbed on its surface. α-MnO_2 was synthesized under the similar reaction condition except that the CFP was sputtered with Pt (Pt/CFP) prior to the reaction and the reaction time was prolonged to 3 h at 150 °C.

Fig. 1 shows X-ray diffraction (XRD) patterns of the obtained products. The diffraction peaks of MnO_2 grown on bare CFP are indexed to δ-MnO_2 (JCPDS 80-1098, monoclinic symmetry with *C*2/*m* space group, lattice parameters of a=5.15 Å, b=2.84 Å, c=7.17 Å), whereas those of MnO_2 grown on Pt/CFP match the peaks from pure α-MnO_2 (JCPDS 44-0141, tetragonal symmetry with *I*4/*m* space group, lattice parameter of a=b=9.78 Å, c=2.86 Å).[10] The basic building block of MnO_2 is [MnO_6] octahedral units. Depending on how these building blocks are interconnected, several polymorphs of MnO_2 can be formed. δ-MnO_2 forms when the [MnO_6] octahedral units assembled into two-dimensional sheets held together with a distance of 0.73 nm. On the contrary, the crystal structure of α-MnO_2 consists of double chains of [MnO_6] octahedral forming 2×2 and 1×1 tunnels with the sizes of 0.46 and 0.189 nm, respectively.[11] It has been known that raising a reaction temperature facilities the anisotropic growth of MnO_2, thus leading to the formation of α-MnO_2.[10] Unlike the previous report, we could not observe the formation of α-MnO_2

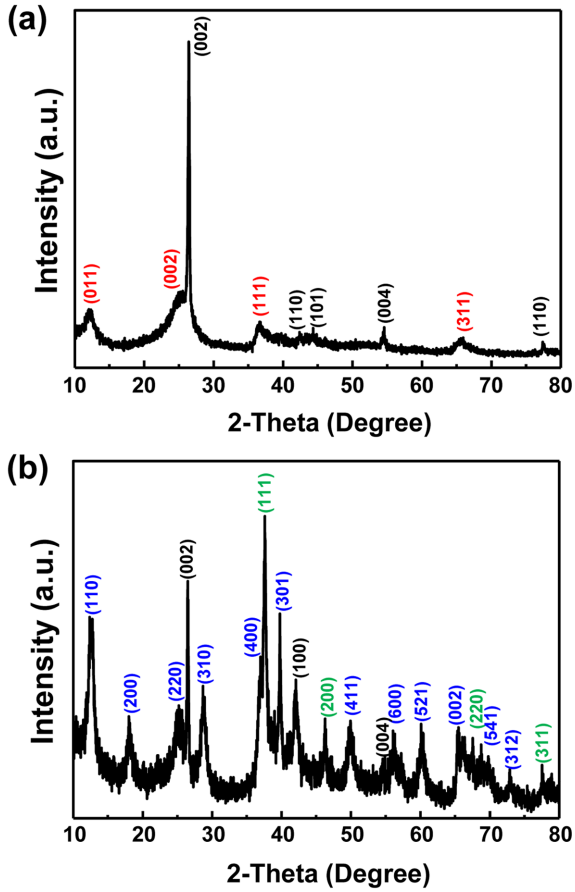

***Figure* 1.** XRD patterns of (a) δ-MnO_2 and (b) α-MnO_2 deposited on CFP and Pt/CFP substrates (peaks from δ-MnO_2, α-MnO_2, Pt, and CFP are shown in red, blue, green, and black, respectively).

even at an elevated temperature (150 °C) when the bare CFP was employed as a substrate. However, the use of the Pt/CFP substrate allowed us to synthesize α-MnO_2 at 150 °C. In general, α-MnO_2 is formed when δ-MnO_2 created at an early stage of the reaction undergoes a phase-transformation at a high temperature. In our synthesis, it is obvious that raising the reaction temperature failed to induce the phase-transformation. Therefore, we concluded that Pt deposited on CFP played a critical role in the formation of α-MnO_2 and facilitated the phase-transformation as a catalyst.

Fig. 2 shows the scanning electron microscopy (SEM) images of δ-MnO_2 and α-MnO_2 deposited on CFP and Pt/CFP substrates, respectively. The entire surface of CFP was fully covered with MnO_2 in both samples. In the case of δ-MnO_2, a myriad of nanoflakes were vertically integrated on top of CFP. On the contrary, one-dimensional, thorn-like nanostructure was observed for α-MnO_2. This difference in the morphology reflects the characteristics of crystal structures of δ-MnO_2 and α-MnO_2. δ-MnO_2 possesses two-dimensional lamellar structure, thus the integration of nanoflakes is favored when it grew on the CFP substrate. However, one-dimensional tunnels feature prominently in α-MnO_2, thus the anisotropic growth results in the formation of nanothorns.

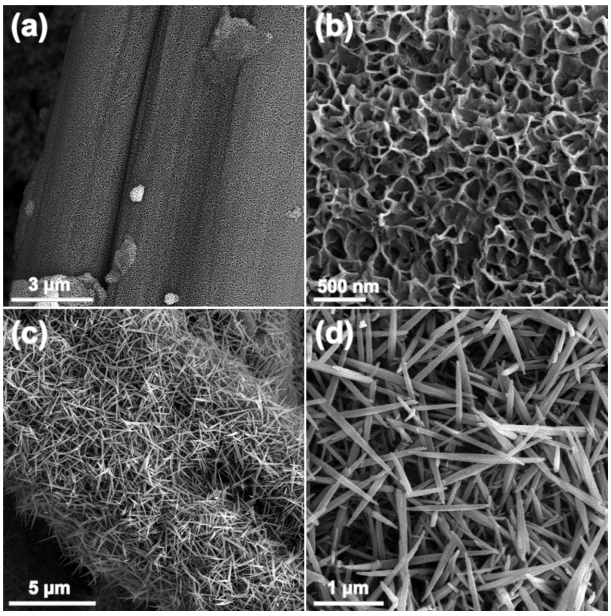

***Figure* 2.** SEM images of (a and b) δ-MnO_2 and (c and d) α-MnO_2 deposited on CFP and Pt/CFP substrates.

This structural difference may have a significant effect on the pseudocapacitance behavior of MnO_2 because the charge storage mechanism of MnO_2 is based on the intercalation and deintercalation of protons or cations through the gap between interlayers in the case of δ-MnO_2 or the nanochannels in the case of α-MnO_2.[12,13] To investigate the effect of the structural difference on pseudocapacitance, δ-MnO_2 deposited on CFP and α-MnO_2 on Pt/CFP were employed as pseudocapacitor electrodes. *Figs.* 3a and 3b show the cyclic voltammograms (CVs) of δ-MnO_2 and α-MnO_2 electrodes at various scan rates. It is well-known that the capacitive behavior of MnO_2 results from the following redox reaction (eq. 1):[14]

$$MnO_2 + M^+ + e^- \leftrightarrow MnOOM \text{ (M: proton or cations)} \quad (1)$$

However, no characteristic redox peaks were observed for both electrodes, implying that the MnO_2 electrodes were charged and discharged at pseudo-constant rates over the entire potential range. This unique feature indicates that the capacitive behavior of both electrodes show a nearly ideal capacitive behavior.[15] The mass-specific capacitances (C_m) of both electrodes were calculated determined from CV curves using the following equation

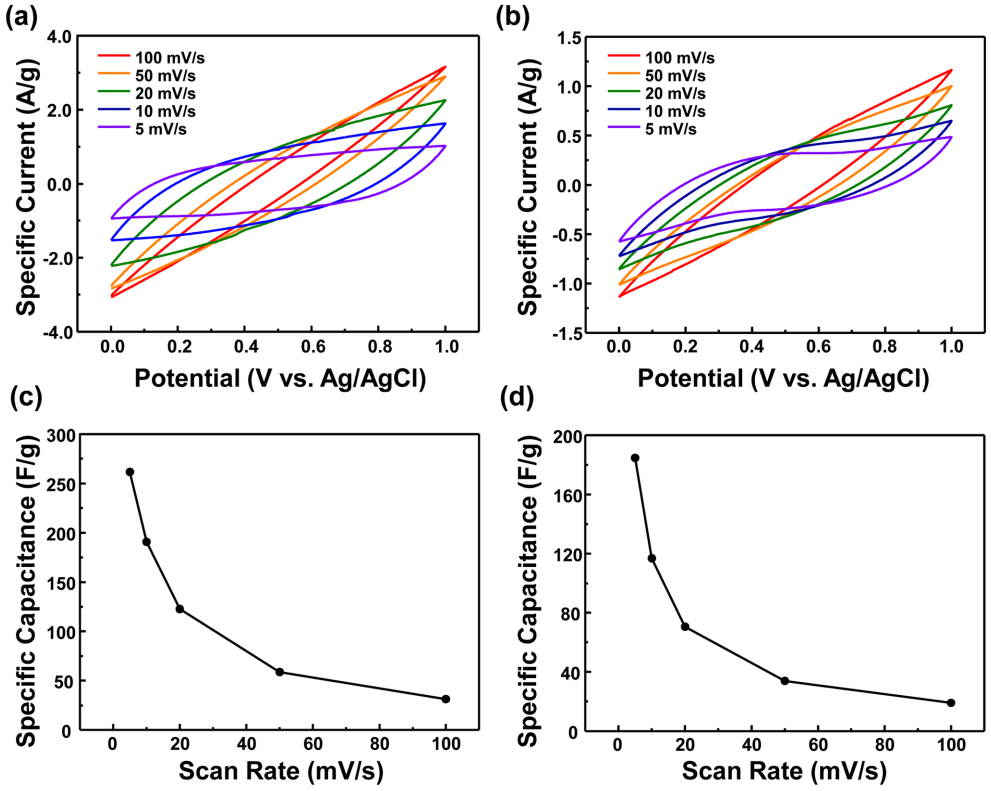

***Figure* 3.** Cyclic voltammograms of (a) δ-MnO_2 and (b) α-MnO_2 in 0.1 M Na_2SO_4 electrolyte at different scan rates; Specific capacitances of (c) δ-MnO_2 and (d) α-MnO_2 as a function of scan rates.

(eq. 2):

$$C_m = \int I \cdot dt/(\Delta V \cdot m) \quad (2)$$

where I is the oxidation/reduction current, dt is the time differential, ΔV is the potential window, and m is the mass of active material.[16] *Figs.* 3c and 3d display the specific capacitances of δ-MnO_2 and α-MnO_2 electrodes at different scan rates. The mass-specific capacitances of δ-MnO_2 were found to be 261.5, 190.8, 122.7, 58.6, and 31.3 F/g at the scan rates of 5, 10, 20, 50, and 100 mV/s, respectively. In the case of α-MnO_2, 184.8, 116.8, 70.7, 33.9, and 19.0 F/g were obtained at each scan rate, respectively. This clearly shows that the specific capacitances of δ-MnO_2 were larger than those of α-MnO_2, which we attributed to the difference in crystallographic structures. δ-MnO_2 possesses a large interlayer gap of 0.73 nm, whereas α-MnO_2 features the nanochannels with tunnel sizes of 0.46 and 0.189 nm. The larger interlayer separation in δ-MnO_2 can facilitate the intercalation and deintercalation of charged species, thus leading to a better capacitor performance as compared to α-MnO_2.

In summary, we demonstrated in this study a simple synthesis route that can allow for a delicate control over the crystal structures of MnO_2. When the bare CFP was employed as a substrate for the growth of MnO_2, δ-MnO_2 was formed. Unlike the previous reports, an elevated temperate was not capable of inducing the phase formation from δ-MnO_2 to α-MnO_2. Upon Pt deposited on the CFP, however, α-MnO_2 was successfully grown even at a mild temperature, which was attributed to the role of Pt as a catalyst for the phase transformation. When evaluated as electrodes for pseudocapacitor, both δ-MnO_2 and α-MnO_2 electrodes showed a nearly ideal capacitive behavior. The mass-specific capacitances of δ-MnO_2 were larger than those of α-MnO_2, which was ascribed to the more ion-accessible crystallographic structure of δ-MnO_2. Given that MnO_2 has various crystal structures (e.g., β-MnO_2, λ-MnO_2) other than δ-MnO_2 and α-MnO_2, we believe that further investigation of the effect of crystallographic structure of MnO_2 on the pseudocapacitance would shed light on this promising energy storage material.

Acknowledgments. This work was supported by a research grant funded by the College of Science and Technology, Hanyang University.

REFERENCES

1. Aricò, A. S.; Bruce, P.; Scrosati, B.; Tarascon, J.-M.; van Schalkwijk, W. *Nat. Mater.* **2005**, *4*, 366–377.
2. Chen, S.; Xing, W.; Duan, J.; Hu, X.; Qiao, S. Z. *J. Mater. Chem. A* **2013**, *1*, 2941–2954.
3. Kim, H.; Fortunato, M. E.; Xu, H.; Bang, J. H.; Suslick, K. S. *J. Phys. Chem. C* **2011**, *115*, 20481–20486.
4. Jiang, J.; Li, Y.; Liu, J.; Huang, X.; Yuan, C.; Lou, X. W. *Adv. Mater.* **2012**, *24*, 5166–5180.
5. Zhao, X.; Zhang, L.; Murali, S.; Stoller, M. D.; Zhang, Q.; Zhu, Y.; Ruoff, R. S. *ACS Nano* **2012**, *6*, 5404–5412.
6. Song, M.-K.; et al. *Nano Lett.* **2012**, *12*, 3483–3490.
7. Li, Q.; Wang, Z.-L.; Li, G.-R.; Guo, R.; Ding, L.-X.; Tong, Y.-X. *Nano Lett.* **2012**, *12*, 3803–3807.
8. Hu, L.; Chen, W.; Xie, X.; Liu, N.; Yang, Y.; Wu, H.; Yao, Y.; Pasta, M.; Alshareef, H. N.; Cui, Y. *ACS Nano* **2011**, *5*, 8904–8913.
9. Choi, B. G.; Yang, M.; Hong, W. H.; Choi, J. W.; Huh, Y. S. *ACS Nano* **2012**, *6*, 4020–4028.
10. Xiao, W.; Wang, D.; Lou, X. W. *J. Phys. Chem. C* **2010**, *114*, 1694–1700.
11. Post, J. E. *Proc. Natl. Acad. Sci. U.S.A.* **1999**, *96*, 3447–3454.
12. Patel, M. N.; Wang, X.; Wilson, B.; Ferrer, D. A.; Dai, S.; Stevenson, K. J.; Johnston, K. P. *J. Mater. Chem.* **2010**, *20*, 390–398.
13. Duay, J.; Sherrill, S. A.; Gui, Z.; Gillette, E.; Lee, S. B. *ACS Nano* **2013**, *7*, 1200–1214.
14. Lei, Z.; Shi, F.; Lu, L. *ACS Appl. Mater. Interfaces* **2012**, *4*, 1058–1064.
15. Yang, L.; Cheng, S.; Ding, Y.; Zhu, X.; Wang, Z. L.; Liu, M. *Nano Lett.* **2011**, *12*, 321–325.
16. Lee, E. J.; Bang, J. H. *Mater. Lett.* **2013**, *105*, 28–31.